



HAL
open science

A cost-efficient Shadow Particle Tracking Velocimetry setup suitable for tracking small objects in a large volume

Peter Huck, Nathanaël Machicoane, Romain Volk

► **To cite this version:**

Peter Huck, Nathanaël Machicoane, Romain Volk. A cost-efficient Shadow Particle Tracking Velocimetry setup suitable for tracking small objects in a large volume. *Procedia IUTAM*, 2017, 20, pp.175 - 182. 10.1016/j.piutam.2017.03.024 . hal-02477858

HAL Id: hal-02477858

<https://hal.science/hal-02477858>

Submitted on 13 Feb 2020

HAL is a multi-disciplinary open access archive for the deposit and dissemination of scientific research documents, whether they are published or not. The documents may come from teaching and research institutions in France or abroad, or from public or private research centers.

L'archive ouverte pluridisciplinaire **HAL**, est destinée au dépôt et à la diffusion de documents scientifiques de niveau recherche, publiés ou non, émanant des établissements d'enseignement et de recherche français ou étrangers, des laboratoires publics ou privés.



24th International Congress of Theoretical and Applied Mechanics

A cost-efficient Shadow Particle Tracking Velocimetry setup suitable for tracking small objects in a large volume

Peter Huck^a, Nathanael Machicoane^b, Romain Volk^{a,*}^aUniv Lyon, Ens de Lyon, Univ Claude Bernard, CNRS, Laboratoire de Physique, F-69342 Lyon, France^bDepartment of Mechanical Engineering, University of Washington, Seattle, WA, USA

Abstract

We use a Shadow Particle Tracking Velocimetry technique (S-PTV) with collimated light to investigate the dynamics of a turbulent von Kármán (VK) flow in water. Such a PTV technique permits easy calibration since the apparent particle positions on the images do not depend on the camera-particle distance and tracking of small objects (100 μm particles, fibers, ...) with low power LEDs light sources is made possible in a large volume (approximately $(6\text{ cm})^3$). This technique provides an ensemble of Lagrangian trajectories which are conditioned in space on a grid in order to reconstruct the 3d Eulerian mean flow together with its fluctuations. Typical Lagrangian statistics can also be obtained with this technique, such as velocity and acceleration auto-correlation functions.

© 2017 The Authors. Published by Elsevier B.V. This is an open access article under the CC BY-NC-ND license

(<http://creativecommons.org/licenses/by-nc-nd/4.0/>).

Peer-review under responsibility of organizing committee of the 24th International Congress of Theoretical and Applied Mechanics

Keywords: Particles in turbulence ; Particle Tracking Velocimetry ; Lagrangian statistics; Inhomogeneous and anisotropic flow

1. Introduction

Turbulent flows play a major role in mixing, chemical process in reactors, and has received much attention over the years. In the field of experimental fluid dynamics research, significant progress has been made during the last decade with the advent of space and time resolved optical techniques based on high-speed imaging¹³. However, classical techniques such as Particle Image Velocimetry reduces the available information (2 or 3 components in a plane) which may impede or complicate a direct resolution of the Eulerian flow, especially when the flow is created in a complex geometry. In this context, Lagrangian techniques such as Particle Tracking Velocimetry, offer the possibility for a full 3d characterization of the flow properties at a modest computational cost^{15,10,13}. By using an ensemble of fast cameras, PTV permits tracking of small particles (10 – 100 μm large) in turbulent flows with Reynolds numbers $R_\lambda > 100$ with a temporal resolution of the order of the Kolmogorov frequency $f_K = \sqrt{\epsilon/\nu} \sim 1 - 10\text{ kHz}$, ϵ being the injected power per unit mass, and ν the fluid viscosity. However when developing a PTV setup with classical illumination, one confronts several difficulties: the quality of images depends strongly on the particle characteristics (refraction index, size), a complex 3d calibration is required in order to achieve stereo-matching between the different camera views¹⁴, and powerful light sources (high power LEDs, or a high power laser) are requisite when tracking

* Corresponding author. Tel.: +33-4-72-72-39-45 ; fax: +33-4-72-72-89-50.

E-mail address: romain.volk@ens-lyon.fr

small objects. To overcome these difficulties we have developed a new optical setup inspired from previous works³ which tracks particles' shadows produced when using parallel lighting.

2. Shadow Particle Tracking setup

2.1. Experimental setup

The experimental apparatus is a von Kármán flow that has been used previously³ with a square cross-section of 15 cm on each side. Two bladed discs of radius $R = 7.1$ cm counter-rotate at constant frequency Ω (figure 1 (a)) and are 20 cm apart. The flow has a strong mean spatial structure arising from the counter rotation of the disks. The azimuthal component resulting from this forcing is of order $2\pi R\Omega$ near the disks' edge and zero in the mid-plane ($z = 0$), creating a strong axial gradient (figure 1 (a)). The disks also act as centrifugal pumps ejecting the fluid radially in their vicinity, resulting in a large-scale poloidal recirculation with a stagnation point in the geometrical centre of the cylinder (figure 1 (b)). Using water to dilute an industrial lubricant, UconTM, a mixture with a viscosity of $8.2 \text{ m}^2\text{s}^{-1}$ and a density of $\rho = 1000 \text{ kg}\cdot\text{m}^{-3}$ allows the production of an intense turbulence with a Taylor-based Reynolds number $R_\lambda = 200$ and a dissipative length $\eta = 130$ microns (see table 1 for more details on the flow parameters). We perform particle tracking of Lagrangian tracers ($250 \text{ }\mu\text{m}$ polystyrene particles with density $\rho_p = 1060 \text{ kg}\cdot\text{m}^{-3}$) in a large volume $6 \times 6 \times 5.5 \text{ cm}^3$ centered around the geometrical centre $((x, y, z) = (0, 0, 0))$ of the flow with 2 high-speed video cameras (Phantom V.12, Vision Research, $1\text{Mpix}@7\text{kHz}$) with a resolution 800×768 pixels, and a frame rate up to $f_s = 12 \text{ kHz}$. Such a sampling frequency is sufficient for resolving particle acceleration, calculated by taking the second derivative of the trajectories.

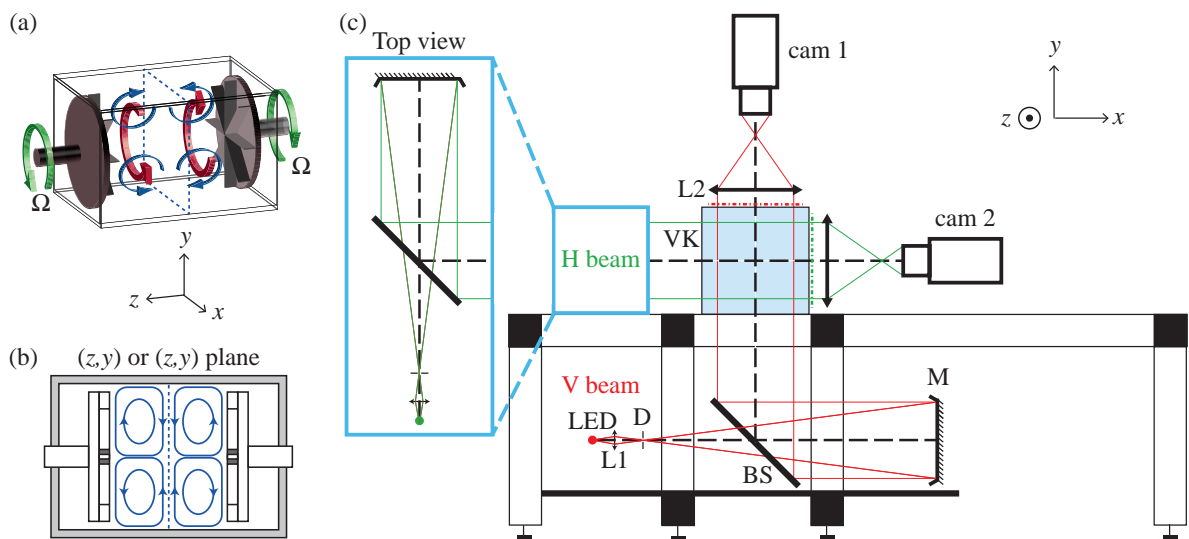


Fig. 1. (a) Sketch of the counter-rotating von Kármán flow. Arrows indicate the topology of the mean flow, the dashed line indicates the mid-plane of the vessel. (b) Schematic cut of the vessel along the (z, x) or (z, y) plane. (c) Optical setup for S-PTV with 2 identical optical arrangements forming an angle $\theta = 90$ degrees (only the vertical arm is described). The 1W LED source is imaged in the focus of a parabolic mirror to form a large collimated beam. A converging lens and a diaphragm are used to make the LED a better point-like source of light. Light is propagating through the flow volume using a beam splitter (BS) before being collected using a 15 cm large lens whose function is to redirect the light into the camera objective of the camera. The optical system $[L_2 + \text{objective}]$ is focussed on the output face of the vessel marked with a dashed-dotted line.

The camera setup is inspired from a previous work³ and is depicted in figure 1 (c). It consists of 2 identical optical configurations with a small LED located at the focal point of a large parabolic mirror (15 cm diameter, 50 cm focal length) forming 2 collimated beams which are perpendicular to each other in the measurement volume. A converging lens and a diaphragm are used to make the LED a better point-like source of light. This large parallel ray of light then reflects on a beam splitter and intersects the flow volume before being collected by the camera sensor using a doublet

consisting of a large lens (15 cm in diameter) and the camera objective. All optical elements are aligned using large (home made) reticules which also precisely measure the magnification in each arrangement. When placing an object in the field of view, it appears as a black shadow on a white background corresponding to the parallel projection of the object on the sensor. The particle size and shape do not depend on the object-to-camera distance, as opposed to classical lighting schemes where the apparent object size is a decreasing function of the object-to-camera distance. When particles are tracked, camera 1 will then provide their (x_1, z_1) 2d positions while camera 2 will measure their (y_2, z_2) positions. The z coordinate is redundant and we have the equation $z_2 = az_1 + b$ where a and b account for slight differences in the magnification and centering between both arrangements, respectively.

Ω	v'_x	v'_y	v'_z	v'	τ_η	η	ϵ	R_λ	Re
Hz	m.s^{-1}	m.s^{-1}	m.s^{-1}	m.s^{-1}	ms	μm	W.kg^{-1}	-	-
4.2	0.39	0.37	0.24	0.34	3.2	162	0.8	175	16200
5.5	0.50	0.49	0.33	0.45	2.1	130	1.9	200	21200
6.9	0.62	0.62	0.41	0.56	1.5	111	3.6	225	26700

Table 1. Parameters of the flow. Ω , rotation rate of the discs; ϵ , dissipation rate obtained from the power consumption of the motors. The rms velocities are obtained at the geometrical centre of the flow using data points situated in a ball with a 1 cm radius. The Taylor-based Reynolds number is estimated as $Re_\lambda = \sqrt{15}v'/\nu\epsilon$ with $v' = \sqrt{(v_x'^2 + v_y'^2 + v_z'^2)}/3$. The large scale Reynolds number is $Re = 2\pi R^2\Omega/\nu$. The kinematic viscosity of the water-UconTM mixture is $\nu = 8.2 \cdot 10^{-6} \text{ m}^2\text{s}^{-1}$ with a density $\rho = 1000\text{kg m}^{-3}$.

2.2. Tracking algorithms

Given the magnification of the setup (1/4, 1px equals 90 μm), the depth of field of the optical arrangement is larger than the experiment. As both beams do not overlap on the entire flow volume, particles situated in one arm but outside the measurement volume can give a well contrasted image on one camera while not being seen by the other. Such a situation could lead to a wrong stereo-matching event when many particles are present. This is illustrated on figure 2 (a), where the shadows left by two particles situated at the exact same z position but outside of the beams overlap (black dots) could be interpreted as one particle within the overlapping region (dashed circle). To mitigate these errors we construct 2d trajectories for each camera using the (x_1, z_1) and (y_2, z_2) coordinates separately. Once tracked in time, these trajectories may be stereo-matched instead of individual particle positions. One may note that while typical PTV algorithms perform stereo-matching on particle positions followed by trajectory construction, we proceed in the opposite order. The advantage of this method is that neither stereo-matching nor tracking errors are made, as will be detailed below. Due to the necessity of trajectory occurrence in the overlapping beam area, one must track many more 2d trajectories than are stereo-matched. One last drawback is the projection of 3d positions into a plane, which strongly decreases the inter-particle distance making apparent particle overlap an issue when the particle diameter becomes large with respect to the effective measurement volume. However, the presence of a redundancy in the z coordinate may be used to overcome such indetermination when the apparent proximity results only from projection.

We implement a 2d tracking scheme using a 4 Frames Best Estimate method inspired from previous works.^{9,8,17} Stereo-matching is then performed by identifying trajectories with $z_1(t) \approx z_2(t)$ using the relation $z_2 = az_1 + b$ as shown in figure 2 (b). This key relation is determined recursively using a dilute ensemble of particles for which an initial identification of a single pair of 2d trajectories allows a first estimate of the relationship between z_2 and z_1 . As more trajectories are found, the affine relationship is refined until the maximum possible amount of trajectories for a single experiment is obtained. In this recursive manner, the tracking algorithm is self-calibrating. Here the parameters are $a = 0.98$, $b = 15.6 \text{ px}$ estimated from 1900 matched trajectories, corresponding to $6 \cdot 10^6$ data points as shown in figure 2 (c). Together with the pixel-to-mm conversion from one of the cameras, this method provides all relevant information about particle positions in laboratory coordinates. By taking only trajectories that are long enough to ensure a proper stereo-matching (typically 70 time-steps, approximately $2.5\tau_\eta$), we prevent the inclusion of any anomalous trajectories. Such an occurrence becomes increasingly unlikely as the trajectory duration threshold is increased. A false trajectory can only occur when the relationship $z_2 = az_1 + b$ leads to an indetermination when particles are close to colliding, an extraordinarily rare event in dilute situations. After tracking and stereo-matching

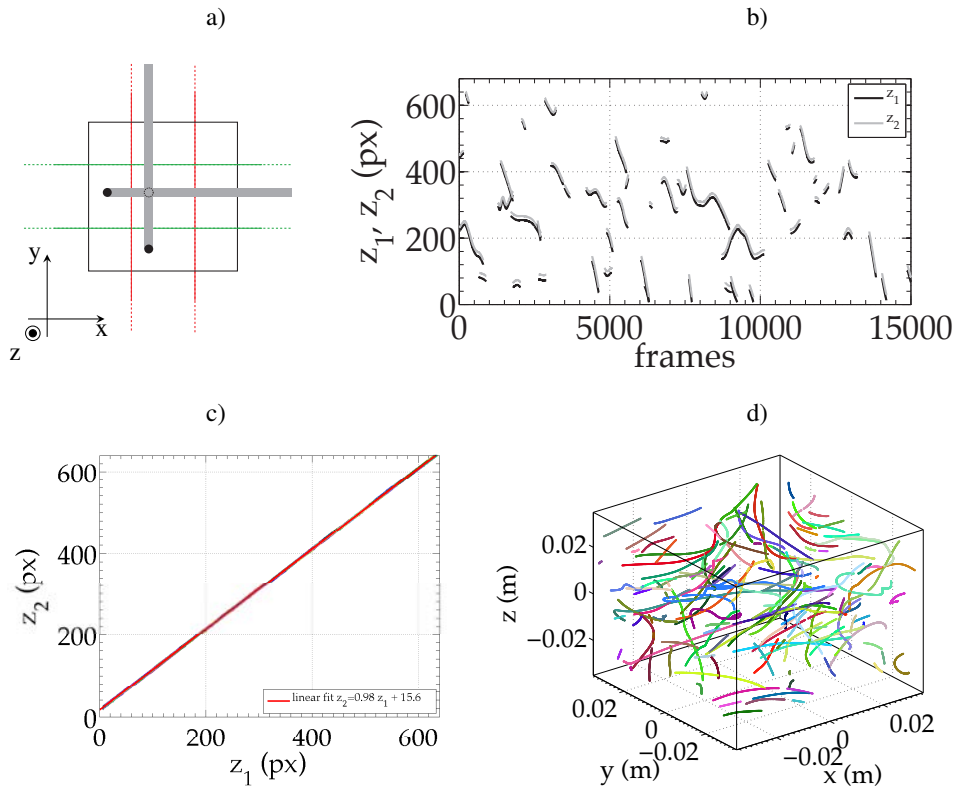


Fig. 2. (a) Scheme of the intersecting parallel light beams showing individual particle stereo-matching is not reliable. The black dots are two particles at the same z position outside of the beam overlapping region and the dashed circle is a particle at the same z position within the region (both situations being measured identically by the cameras). (b) Time evolution of the raw z (redundant) coordinate of the same particles as obtained with 2d tracking with cam1 and cam2. Only 38 matched trajectories are plotted. (c) Affine relation between $z_2 = az_1 + b$ ($a = 0.98$, $b = 15.6$ px) measured with 1900 trajectories corresponding to $6 \cdot 10^5$ data points. (d) Random sample of 150 trajectories in the vessel obtained from the same movie.

each pair of movies gives an ensemble of trajectories from which all single particle statistics can be computed as shown in figure 2 (d).

3. Flow measurements

The measurement volume ($6 \times 6 \times 5.5$ cm³) covers more than an integral scale ($L_V = v'^3 \epsilon^{-1} \approx 4.8$ cm) in all directions, rendering it inhomogeneous and necessitating a sufficient number of trajectories to converge spatially and temporally conditioned statistics. We record 200 pairs of movies with a duration of 1.3 seconds at 12kHz and obtain $O(1000)$ tracer trajectories per film. A statistical ensemble of $O(10^5)$ trajectories with mean durations $\langle t \rangle \sim 0.25/\Omega$ permits the spatial convergence of both Eulerian and Lagrangian statistics. The flow properties are obtained from the PTV data and are given in table 1 together with the energy dissipation ϵ which is estimated globally from the power consumption of the motor.¹⁶ The fluctuating velocity of the flow is found to be proportional to the propeller frequency Ω (table 1) which is because the flow is produced by inertial steering using bladed discs and the turbulence becomes fully developed, provided $Re = \frac{2\pi R^2 \Omega}{\nu} > 4000$ ¹¹. In what follows, we focus our analysis on $\Omega = 5.5$ Hz.

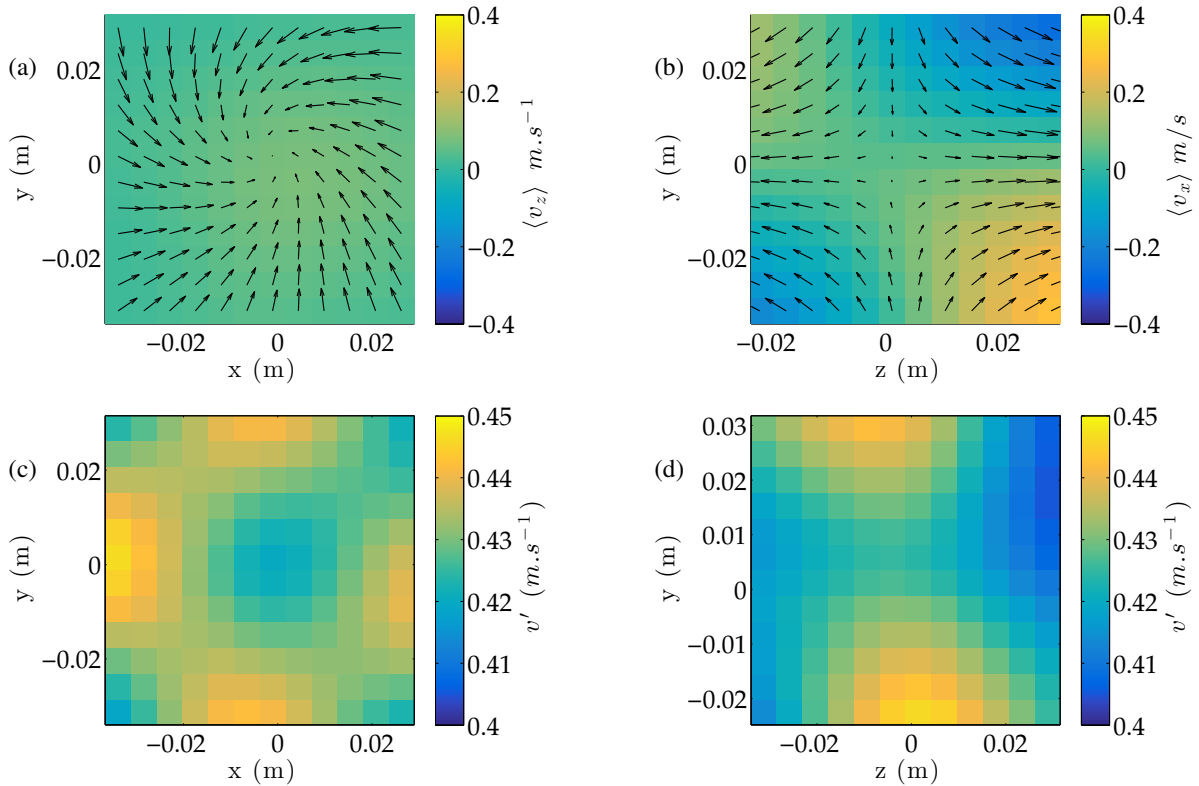


Fig. 3. Cuts of the 3d reconstructed Eulerian mean velocity (a,b) field and rms velocity (c,d). The reconstruction is achieved by computing the mean $\langle \vec{v} \rangle$ and rms values (v'_x, v'_y, v'_z) of the velocity in each bin of a 12^3 cartesian grid. (a) $\Pi_{xy} = (x, y, z = 0)$ plane. Arrows are $(\langle v_x \rangle, \langle v_y \rangle)$, the color coding for the $\langle v_z \rangle$. (b) $\Pi_{yz} = (x = 0, y, z)$ plane. Arrows are $(\langle v_y \rangle, \langle v_z \rangle)$, the color coding for the $\langle v_x \rangle$. (c) rms value of velocity fluctuations $v' = \sqrt{(v'_x)^2 + v'_y{}^2 + v'_z{}^2}/3$ in the $\Pi_{xy} = (x, y, z = 0)$ plane. (d) rms value of velocity fluctuations in the $\Pi_{yz} = (x = 0, y, z)$ plane.

3.1. 3d Eulerian flow

The 3d particle tracking yields a set of trajectories, each containing the temporal evolution of Lagrangian velocity at the particle position. Based on this ensemble of trajectories, one may reconstruct the mean velocity field in 3d $\langle \vec{v} \rangle(x, y, z) = (\langle v_x \rangle, \langle v_y \rangle, \langle v_z \rangle)$ and the rms fluctuations of each velocity component (v'_x, v'_y, v'_z). This is achieved by an Eulerian conditioning of the Lagrangian dataset on a 12^3 cartesian grid, which corresponds to a spatial resolution of 5 mm in each direction. The choice of the grid size must satisfy several criteria: it must be small as compared to the typical scale of the mean flow properties (here $L_v \sim 4.8$ cm), but large enough so that statistical convergence is achieved. Here the grid size was chosen so that there are at least $\mathcal{O}(1000)$ trajectories across each bin which is enough to converge both the mean and rms values.

Figure 3(a,b) display two cross-sections of the reconstructed mean flow in two perpendicular planes, the mid plane $\Pi_{xy} = (x, y, z = 0)$ and $\Pi_{yz} = (x = 0, y, z)$, an horizontal plane containing the axis of rotation of the discs. We observe for the mean flow a structure that is close to the schematic view of figure 1 (a). The flow is almost radial and convergent with $\langle v_z \rangle \sim 0$ in Π_{xy} , with a z component which reverses under the transformation $z \rightarrow -z$ (figure 3(b)). We also observe a strong y -component of the velocity in Π_{yz} which reverses under the transformation $y \rightarrow -y$ and corresponds to the differential rotation imposed by the discs. These cross-sections also reveal that the flow has the topology of a stagnation point at the geometric centre $(0, 0, 0)$ as was shown in another von Kármán flow with a circular section⁶. With a 3d measurement of the mean flow, it is possible to compute spatial derivatives along all

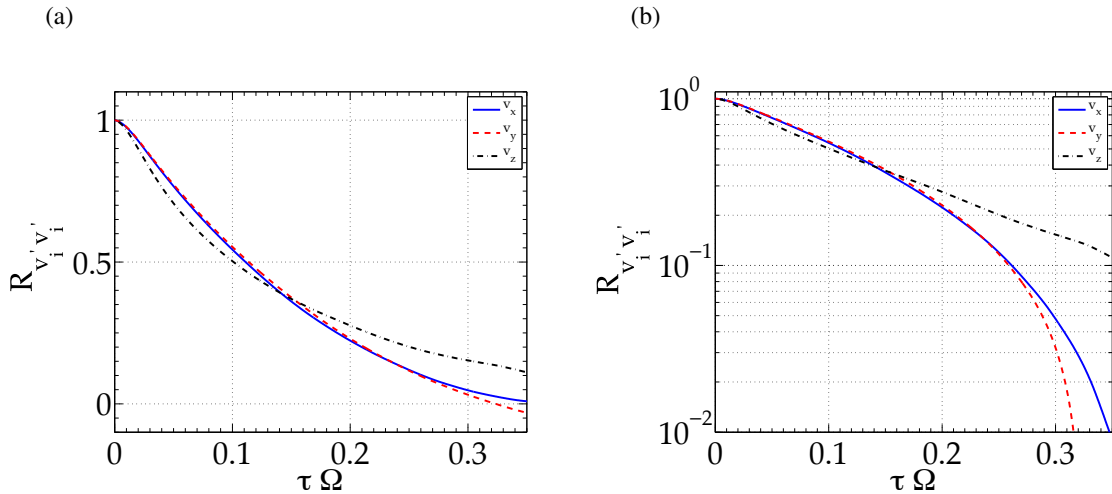


Fig. 4. Normalized velocity auto-correlation functions for the three components versus the normalized time-lag $\Omega\tau$. (a) plotted in linear scale. (b) plotted with semilog vertical scale. Solid line: x-component. Dashed line: y-component. Dashed dotted line: z-component.

directions. This leads to $\partial_x \langle v_x \rangle \sim \partial_y \langle v_y \rangle \approx -1.5 \Omega$ for the stable directions, and $\partial_z \langle v_z \rangle \sim 3.0 \Omega$ for the unstable direction. Note that the sum of these terms must be zero because this quantity is the divergence of the mean flow. This condition is found to be well satisfied although the velocity components were computed independently without any constraint. Verifying that the flow is divergence free is then an *a posteriori* test that the reconstruction of the mean flow is physical.

Figure 3(c,d) display rms values of velocity fluctuations $v' = \sqrt{(v_x'^2 + v_y'^2 + v_z'^2)}/3$ in $\Pi_{xy} = (x, y, z = 0)$ and $\Pi_{yz} = (x = 0, y, z)$. These maps reveal that the flow properties are non isotropic and non homogeneous at large scale, as already observed in similar setups (reference² for instance). We observe that the fluctuations increase with $r = \sqrt{x^2 + y^2}$ in the Π_{xy} plane, the fluctuation map having the square symmetry of the vessel. An interesting result is that as opposed to what is observed in the x and y directions, the flow properties are only weakly varying in the z direction as can be seen in the Π_{yz} plane. These different behaviors will have strong consequences on the shape of the Lagrangian velocity auto-correlation functions.

3.2. Lagrangian two-time statistics

The Lagrangian velocity auto-correlation function is a fundamental quantity when addressing particle dispersion from a point source¹². However, computing this quantity requires long trajectories. As a consequence, particles will explore regions with strong mean flow variations, making it impossible to properly estimate the turbulent Lagrangian integral time-scale⁵. The 3d mean field has low levels of noise and sufficient resolution to permit its subtraction step-by-step along each trajectory to obtain signal comprised solely of velocity fluctuations $v_i'(\vec{X}(t)) = v_i(\vec{X}(t)) - \langle v_i \rangle(\vec{X}(t))$, with $i = x, y, z$. Here, $\langle v_i \rangle(\vec{X}(t))$ are the components of the 3d Eulerian mean-field at the particle position for time t , $\vec{X}(t)$. These trajectories of fluctuating velocity are then used to estimate the velocity correlations as $R_{v_i v_i}(\tau) = \langle v_i'(t + \tau) v_i'(t) \rangle / \langle v_i'^2 \rangle$, where τ is the time-lag. To allow for comparison with measurements in similar setups (but with a circular cross-section), we only use $2.5 \cdot 10^4$ trajectories which have crossed through a sphere with a diameter of 2 cm in the center of the vessel.

Figure 4 (a) displays the velocity auto-correlation function for the three components up to $\tau\Omega = 0.35$ corresponding to $\tau/\tau_\eta = 30$. We only observe a total decorrelation for the two transverse components x, y , while the axial component is correlated on a longer time-scale, as has already been observed¹⁰. The semi-log graph of figure 4 (b) demonstrates that only the axial component is exponentially decreasing on long times, which is what is observed in homogeneous and isotropic turbulence¹⁸. This must be linked to the fact that the fluctuations are more homogeneous in the z

direction than in any other so that the properties of v'_z do not vary much along the trajectories when computing $R_{v'_z v'_z}(\tau)$. Because the shape of the correlation function depends on the components, we do not fit any function to estimate the Lagrangian integral time-scale, but compute it as $T_i = 1/f_s \sum R_{v_i v_i}$ up to $\tau\Omega = 0.55$ which is sufficient to observe a total decorrelation of v'_z . We obtain ratios between the injection time-scale and the integral times $1/T_z\Omega = 6.7$ and $1/T_x\Omega = 7.7$, similar to values ranging from 5.4 to 6.2 with varying propeller frequency as found previously in a similar setup with a circular cross-section⁷.

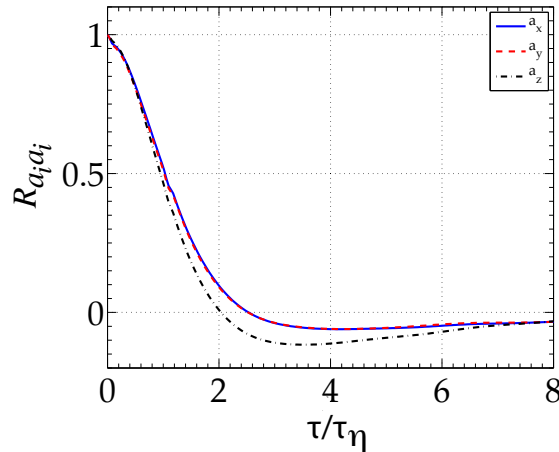


Fig. 5. Normalized acceleration auto-correlation functions for the three components versus the normalized time-lag τ/τ_η . Solid line: x-component. Dashed line: y-component. Dashed dotted line: z-component.

We now probe smaller scale statistics by considering $R_{a_i a_i}(\tau) = \langle a_i(t + \tau)a_i(t) \rangle / \langle a_i^2 \rangle$, the acceleration auto correlation functions. They are computed without subtracting the mean acceleration field thanks to the scale separation between a'_i and $\langle a_i \rangle(\vec{X}(t))$, which are correlated on a time-scale $\tau_a \sim \tau_\eta$ and $T_i \gg \tau_\eta$ respectively. The results are plotted as functions of τ/τ_η in figure 5. While the transverse components x and y are identical at these scales, a small scale anisotropy persists as the axial z component is correlated over shorter time. This is consistent with measurements of acceleration spectra in a similar setup which were shown to be anisotropic even at the highest frequencies¹⁰. Because the integral of the acceleration auto-correlation function has to be zero (the velocity is bounded), we compute the acceleration time-scale using the positive part of the function $t_a^i = \int_0^{\tau_0} R_{a_i a_i} d\tau$, where τ_0 is the first zero-crossing time of $R_{a_i a_i}$. We obtain $t_a^{x,y}/\tau_\eta \sim 2.5$ and $t_a^z/\tau_\eta \sim 2$, yielding an anisotropy ratio of almost 25%, larger than the one associated to the larger velocity scales of approximately 15%. Such an anisotropy must be connected to the stagnation point topology of the mean flow, z being the unstable direction while x, y are stable directions. However, one may observe that the averaged acceleration time-scale $t_a = \sum t_a^i/3 \approx 2.3\tau_\eta$ is close to the famous zero-crossing at $2.2\tau_\eta$ found in homogeneous isotropic turbulent flows.

4. Conclusion

In this contribution we have introduced a novel method for measuring the Lagrangian statistics of small particles or tracers in a highly turbulent flow known to be both inhomogeneous and anisotropic and which may be conditioned in space to reconstruct the Eulerian flow properties in 3d. The Shadow Particle Velocimetry setup, based on two large, perpendicular collimated rays of light requires two LEDs, instead of a high-power laser, and allows for the tracking of small objects in a large volume. The tracking algorithms implement an innovative one-component redundancy to overcome the difficulty of a large depth of field and prevents any wrong trajectory constructions. This setup yields long, clean trajectories necessary to study one-particle dispersion in turbulence and the properties of a flow that is anisotropic both at large and small scales. The technique is tested by computing the velocity and acceleration auto-correlation functions which present time scales in accord with those found in the literature. By using many trajectories,

we are capable of reconstructing a 3d map of ensemble-averaged Eulerian quantities. This versatile setup may also be used with fewer particles to study flow statistics at long times⁴ as is usually done with 1d (or 2d) measurements¹. As the method measures two projections of the objects advected by the flow in two perpendicular planes, it is also suitable to study the translation and rotation dynamics of non-spherical objects, such as fibers or disks.

Acknowledgements

This work is supported by French research programs ANR-12-BS09-0011, ANR-13-BS09-0009 and projet Emergent PALSE/2013/26. Contribution from the European project EuHIT - European High-performance Infrastructures in Turbulence - is also acknowledged.

References

1. de la Torre, A. and Burguete, J. (2007). Slow Dynamics in a Turbulent von Kármán Swirling Flow. *Physical Review Letters*, 99(5):3–6.
2. Faranda, D., Pons, F. M. E., Dubrulle, B., Daviaud, F., Saint-Michel, B., Herbert, É., and Cortet, P.-P. (2014). Modelling and analysis of turbulent datasets using auto regressive moving average processes. *Physics of Fluids (1994-present)*, 26(10):105101.
3. Machicoane, N., Bonaventure, J., and Volk, R. (2013). Melting dynamics of large ice balls in a turbulent swirling flow. *Physics of Fluids*, 25:125101.
4. Machicoane, N., López-Caballero, M., Fiabane, L., Pinton, J.-F., Bourgoïn, M., Burguete, J., and Volk, R. (2016). Stochastic dynamics of particles trapped in turbulent flows. *Phys. Rev. E*, 93:023118.
5. Machicoane, N. and Volk, R. (2016). Lagrangian velocity and acceleration correlations of large inertial particles in a closed turbulent flow. *Physics of Fluids*, 28(3):035113.
6. Monchaux, R., Ravelet, F., Dubrulle, B., Chiffaudel, A., and Daviaud, F. (2006). Properties of steady states in turbulent axisymmetric flows. *Physical Review Letters*, 96:124502.
7. Mordant, N., L  v  que, E., and Pinton, J.-F. (2004). Experimental and numerical study of the Lagrangian dynamics of high Reynolds turbulence. *New Journal of Physics*, 6:116.
8. Ouellette, N. (2006). *Probing the statistical structure of turbulence with measurements of tracer particle tracks*. PhD thesis, Cornell University.
9. Ouellette, N. T., Xu, H., and Bodenschatz, E. (2006a). A quantitative study of three-dimensional lagrangian particle tracking algorithms. *Experiments in Fluids*, 40(2):301–313.
10. Ouellette, N. T., Xu, H., Bourgoïn, M., and Bodenschatz, E. (2006b). Small-scale anisotropy in Lagrangian turbulence. *New Journal of Physics*, 8.
11. Ravelet, F., Chiffaudel, A., and Daviaud, F. (2008). Supercritical transition to turbulence in an inertially driven von karman closed flow. *Journal of Fluid Mechanics*, 601:339–364.
12. Taylor, G. I. (1922). Diffusion by continuous movements. *Proc. Lond. Math. Soc.*, 20:196–212.
13. Tropea, C., Yarin, A., and Foss, J. F., editors (2007). *Springer Handbook of Experimental Fluid Dynamics*. Springer-Verlag Berlin-Heidelberg.
14. Tsai, R. (1987). A versatile camera calibration technique for high accuracy 3d machine vision metrology using off-the-shelf tv cameras and lenses. *IEEE T. Robot. Autom.*, RA-3:323.
15. Virant, M. and Dracos, T. (1997). {3D} {PTV} and its application on lagrangian motion. *Measurement science and technology*, 8:1539–1552.
16. Volk, R., Calzavarini, E., Leveque, E., and Pinton, J.-F. (2011). Dynamics of inertial range particles in a turbulent flow. *Journal of Fluid Mechanics*, 668:223–235.
17. Xu, H. (2008). Tracking Lagrangian trajectories in position-velocity space. *Measurements Science and Technologie*, 19(7):075105.
18. Yeung, P. K. (2001). Lagrangian characteristics of turbulence and scalar transport in direct numerical simulations. *Journal of Fluid Mechanics*, 428:241–274.